

Highly Embedded $8\mu\text{m}$ cores of Star Formation in the Spiral Arms and Filaments of 15 Nearby Disk Galaxies

Bruce G. Elmegreen¹, Debra Meloy Elmegreen²

ABSTRACT

Spitzer Space Telescope observations of 15 spiral galaxies show numerous dense cores at $8\mu\text{m}$ that are revealed primarily in unsharp mask images. The cores are generally invisible in optical bands because of extinction, and they are also indistinct at $8\mu\text{m}$ alone because of contamination by more widespread diffuse emission. Several hundred core positions, magnitudes, and colors from the four IRAC bands are measured and tabulated for each galaxy. The larger galaxies, which tend to have longer and more regular spiral arms, often have their infrared cores aligned along these arms, with additional cores in spiral arm spurs. Galaxies without regular spirals have their cores in more irregular spiral-like filaments, with typically only one or two cores per filament. Nearly every elongated emission feature has $8\mu\text{m}$ cores strung out along its length. The occurrence of dense cores in long and thin filaments is reminiscent of filamentary star formation in the solar neighborhood, although on a scale 100 times larger in galaxies. The cores most likely form by gravitational instabilities and cloud agglomeration in the filaments. The simultaneous occurrence of several cores with regular spacings in some spiral arms suggests that in these cases, all of the cores formed at about the same time and the corresponding filaments are young. Total star formation rates for the galaxies correlate with the total embedded stellar masses in the cores with an average ratio corresponding to a possible age between 0.2 Myr and 2 Myr. This suggests that the identified cores are the earliest phase for most star formation.

Subject headings: stars: formation — ISM: structure — galaxies: ISM — galaxies: spiral — galaxies: star formation

¹IBM Research Division, T.J. Watson Research Center, 1101 Kitchawan Road, Yorktown Heights, NY 10598; bge@us.ibm.com

²Department of Physics & Astronomy, Vassar College, Poughkeepsie, NY 12604

1. Introduction

Spitzer Space Telescope InfraRed Array Camera (IRAC) images of M100 show regularly spaced $8\mu\text{m}$ peaks in the main spiral arms, suggesting that star formation began by gravitational collapse in dense gas compressed into thin dust lanes by stellar spiral arm shocks (Elmegreen et al. 2018, hereafter Paper I). Such shocks were originally modeled by Roberts (1969). Their gravitational fragmentation into massive cloud complexes was considered early on by Elmegreen (1979), Cowie (1981), Balbus & Cowie (1985), and Tomisaka (1987). Cloud-forming instabilities inside swing-amplified spirals, which are themselves the result of separate instabilities in two dimensions (Goldreich & Lynden Bell 1965; Toomre 1981), were shown analytically for magnetic gas by Elmegreen (1994) and simulated by Kim & Ostriker (2001), Kim et al. (2002a) and Kim & Ostriker (2007). Spiral arm formation was recently reviewed by Dobbs & Baba (2014) and Shu (2016).

A related process is the formation of interarm spurs downstream from an unstable spiral arm shock (Balbus 1988), and the fragmentation of these spurs to form massive clouds, as modeled by Kim & Ostriker (2002b). In three-dimensional models of local density wave shocks by Kim & Ostriker (2006), spur formation begins inside the shock with regular condensations and then evolves to make more condensations in the spurs downstream. Galaxy-wide spur formation in two dimensions was first simulated by Chakrabarti (2003), who emphasized ultraharmonic resonances, and Shetty & Ostriker (2006), who highlighted the magneto-hydrodynamic instabilities. Regularly-spaced spiral arm condensations and spurs were also found by Dobbs (2008) in both their non-self-gravitating and self-gravitating models; at low gas surface density ($4 M_{\odot} \text{pc}^{-2}$), the condensations formed by cloud agglomeration with a characteristic separation given by the epicycle radius, and at high surface density ($20 M_{\odot} \text{pc}^{-2}$) they formed by gravitational instabilities that enhanced and focussed cloud agglomeration. (Khoperskov et al. 2013) modeled cloud formation and molecular chemistry in self-gravitating gas shocked by stellar spiral arms; cloud formation was initiated by shear instabilities and then cloud growth followed by agglomeration.

Self-gravitating simulations at sub-pc resolution by Renaud et al. (2013, 2014) made spiral arms with regularly spaced gas clouds; they suggested that the arms fragmented by gravitational instabilities, although possible contributions from the Kelvin-Helmholtz instability were considered also (related to the wiggle instability in Wada & Koda 2004). Analytical models of magnetic spiral arm instabilities are in Lee & Shu (2012) and Inoue & Yoshida (2018, 2019). Simulations of spiral arms in proto-planetary disks also show collapse into cores (Kratte & Lodato 2016).

Gravitational instabilities in local filaments (e.g., Rosanno 1978; Schneider & Elmegreen 1979; André 2017), including long Milky Way dust clouds that may be spiral arm shocks

(e.g. Goodman et al. 2014; Ragan et al. 2014; Mattern et al. 2018), should have a fastest growing mode consisting of regularly-spaced condensations with a characteristic separation proportional to the filament width, depending on magnetic field strength and the equation of state (e.g., Chandrasekhar & Fermi 1953; Stodólkiewicz 1963; Nagasawa 1987; Inutsuka & Miyama 1992; Nakamura et al. 1993; Tomisaka 1995; Fiege & Pudritz 2000; Seo & Youdin 2016; Kainulainen et al. 2016; Clarke et al. 2017; Lou & Hu 2017; Hosseinirad et al. 2018; Chira et al. 2018). This regularity in spiral arms was first measured in 23 galaxies by Elmegreen & Elmegreen (1983), who concluded that the associated cloud complexes have masses comparable to the turbulent Jeans mass of $\sim 10^7 M_{\odot}$. Such giant clouds were also identified in the first quadrant of the Milky Way by Elmegreen & Elmegreen (1987), following earlier work on regularly spaced giant HI clouds in the outer Milky Way by McGee & Milton (1964). Recent studies by Koo et al. (2018) traced these clouds in the Perseus and Outer Milky Way arms.

Most giant molecular clouds in the Milky Way are clustered together in the inner regions of giant HI clouds that are also distributed along the spiral arms (Elmegreen & Elmegreen 1987; Grabelsky et al. 1987), suggesting there is a cascade of collapse from spiral arm shocks to dense star-forming cores. Observations of GMCs alone or of the interstellar medium on scales of ~ 1 kpc or less do not usually reveal the larger regularities that might be associated with spiral arms, nor do conventional observations of star formation in other galaxies, where extinction and young stellar feedback can confuse the process. Other studies of this regularity include the giant star-forming regions in a long and thin tidal shock at mid-radius in the interacting galaxies NGC 2207 and IC 2163 (Elmegreen et al. 2006), and in the spiral arms of M31 (Efremov 2010) and NGC 628 (Gusev & Efremov 2013), which is also one of our galaxies here.

This paper examines 15 galaxies to look for small infrared emission peaks like those in M100. They are revealed here primarily in unsharp mask images made by dividing the IRAC $8\mu\text{m}$ image at $2.4''$ (FWHM) resolution by a blurred version of the same image. This division removes the extended emission. Section 2 discusses our method for identification and measurement, Section 3 compiles observations of the core colors and magnitudes, Section 4 compares core properties for different types of galaxies, Section 5 discusses the implications for star formation, and Section 6 summarizes our conclusions.

2. Observations

Galaxies in the SINGS (Kennicutt et al. 2003) and KINGFISH (Kennicutt et al. 2011) surveys plus M83 (NGC 5236) from the Spitzer Space Telescope archives were selected for low

inclination, large angular size, and diversity of spiral structure. The galaxies span Hubble types from Sab through Sm. Spiral arm classes, which generally correlate with galaxy mass, span the range from flocculent to multiple arm to grand design. The post-Basic Calibrated Data (BCD) processed images in all four IRAC bands ($3.6\mu\text{m}$, $4.5\mu\text{m}$, $5.8\mu\text{m}$, and $8.0\mu\text{m}$) and the $24\mu\text{m}$ MIPS images were retrieved as FITS files and then aligned through the Image Reduction Analysis Facility (IRAF) task *wregister*. Figure 1 shows the 15 galaxies with color IRAC images made using the software package DS9. Each is a composite of the archived $3.6\mu\text{m}$ (in blue), $4.5\mu\text{m}$ (in green), and $8\mu\text{m}$ (in red) images. Table 1 lists key properties of the 15 chosen galaxies, with GSR distance, distance modulus, Hubble type, and radius R_{25} in arcmin and kpc from the NASA/IPAC Extragalactic Database (NED)¹. The table also includes the parsec scale for one arcsecond, Arm Class from Elmegreen & Elmegreen (1987b), star formation rate (SFR) from Thilker et al. (2007) or Kennicutt et al. (2011) as indicated, and number of chosen cores as discussed below. The scale indicates that even though the features found here are relatively small in our images, corresponding to $3''$ diameters, they are still large compared to giant molecular clouds in most galaxies.

In a first step of our analysis, the $8\mu\text{m}$ images were divided by the corresponding $24\mu\text{m}$ images using the IRAF task *imarith*, and displayed as grayscale images in DS9. This was the procedure used in Paper I. This process results in a type of unsharp mask image, since the lower resolution of the $24\mu\text{m}$ image compared with the $8\mu\text{m}$ is approximately equivalent to blurring the original $8\mu\text{m}$ image. A small adjustment of contrast and brightness then usually reveals a network of small bright cores in the arms, spurs, shells, and other filamentary structures. The result for NGC 628 is on the left in Figure 2. Some of the $8\mu\text{m}$ cores have large black regions around them where the $24\mu\text{m}$ emission was particularly bright or large compared to the $8\mu\text{m}$ emission. Recall that the $24\mu\text{m}$ images have an angular resolution three larger than the $8\mu\text{m}$ images, so features with the same physical size and brightness in the two frames would end up looking like a top hat, i.e., a peak in the center the size of the $8\mu\text{m}$ resolution ($2.4''$) and a valley in a ring around the center the size of the $24\mu\text{m}$ resolution ($7.1''$).

A more revealing procedure is an unsharp mask made by dividing the $8\mu\text{m}$ image by a blurred version of the same $8\mu\text{m}$ image using the IRAF task *gauss* with a 3 pixel **sigma**. The right-hand panel in Figure 2 shows the result of this. Clearly the small-scale $8\mu\text{m}$ structure shows up better than in the $8\mu\text{m}/24\mu\text{m}$ image because the background is more uniform. The cores are present in both but in the outer regions they are more evident in the right-hand image. In what follows, we use this second procedure to identify $8\mu\text{m}$ cores.

¹<https://ned.ipac.caltech.edu/>

Unsharp masks are a highly selective process, designed to emphasize a certain angular scale. Nevertheless, we use this process because the features of interest are not easily seen in the $8\mu\text{m}$ or $24\mu\text{m}$ images alone (nor in the other IRAC bands), and they are also not in optical images (Paper I). This does not mean they cannot be seen at $8\mu\text{m}$; in fact most individual cores can be seen as peaks in the 8μ image if the contrast is tuned for that core, but this optimum contrast is generally different for each $8\mu\text{m}$ emission region because the peak intensities and background levels differ. Thus, division by the $8\mu\text{m}$ or $24\mu\text{m}$ images also normalizes the backgrounds to an approximately constant value, and then the IR cores are all visible in a single image where their relative positions and importance for star formation can be assessed.

For each galaxy, we measured clearly visible $8\mu\text{m}$ cores in all four IRAC passbands. The selection effects in unsharp masking imply that distribution functions for luminosity, mass, and size only show the selected parts of more complete functions. For example, the selected core luminosities and sizes increase with galaxy distance (Sect. 4). Still, the tabulated positions of the $8\mu\text{m}$ cores, and their relationships to spiral arms and other structures, can provide clues about their formation. These tabulations can also be a useful guide to other observations, such as molecular gas at arcsecond resolution, which will be necessary to study the associated cloud densities and kinematics.

In total for the 15 galaxies, over 8300 IR cores were identified. The IRAF task *phot* was used with DS9 to find the position of each $8\mu\text{m}$ peak, manually moving the computer cursor to each one and placing it in the central pixel of the peak as viewed in the magnified cutout of the peak’s neighborhood. A list of all the selected positions was made in this way, followed by a plot of these positions as blue dots on a blank field. This plot was then overlaid on the unsharp mask image using Adobe Photoshop, after scaling it to the same size so that each plotted dot covered the $8\mu\text{m}$ peak. The overlay was examined for peaks that were overlooked, and the positions of these peaks were measured and added to the list. After a few iterations of this procedure, most of the small $8\mu\text{m}$ peaks were noted and tabulated. We avoided choosing extended or diffuse emission regions but only picked the small, essentially unresolved peaks. Automatic searching for the peaks with SExtractor failed to find them consistently, as they all have different backgrounds and intensities and are often parts of larger features and filaments that SExtractor finds instead.

Figures 3 to 7 show unsharp mask images with and without blue dots, using selection criteria for $8\mu\text{m}$ cores that are discussed in Section 3. A comparison between the two images reveals a tiny $8\mu\text{m}$ emission peak in the left-hand figure for each blue dot in the right-hand figure. Emission peaks without blue dots were either too faint to be systematically studied or star-like (see below).

3. Properties of $8\mu\text{m}$ Cores

Magnitudes of the $8\mu\text{m}$ peaks were determined in the four IRAC bands using the IRAF task *phot* with a measurement aperture of 2 pixels radius ($3.0''$ diameter, which encompasses the IR cores that stand out in the unsharp mask images), and background subtraction from an annulus between 3 and 4 pixels away from the core center. The zeropoints for conversion of counts to Vega-system magnitudes in each filter were taken from the IRAC Instrument handbook². The right ascension, declination, magnitude and error for each filter, along with the colors for each core, are listed in Tables 2 to 16.

The distributions of $8\mu\text{m}$ apparent magnitudes are shown in Figure 8. They are in a fairly narrow range, from about 13 to 15 mag, for all of the galaxies as a result of the unsharp mask selection. The distributions have long tails at the faint ends that are unphysical and suffer from incompleteness and confusion with noise. To have a representative catalog for future use, we placed a lower limit on the peak brightness of 16 mag, which is 1 to 3 magnitudes fainter than the peak. The measured cores that are fainter than these cutoffs (and other cores that are discarded as well, see below) have a cyan color for that part of the histogram in the figure. The red histograms for NGC 1566 and NGC 5194 are for the cores in the two main spiral arms, which are brighter than the others (Sect. 5.1).

Measurements of NGC 4625 using a 3 pixel radius aperture with a background annulus of 4 to 5 pixels, instead of an aperture radius of 2 pixels as in the figures, had slightly brighter magnitudes (less than in proportion to the larger areas) because most of the cores are extended with diffuse infra-red emission surrounding them. Thus the tabulated magnitudes do not reflect the total light from the whole star-forming region but only the light from the inner 4π square pixels of area, which corresponds to 7.07 arcsec^2 . They are therefore related to the core central surface brightness, which equals $[8.0] + 2.12$ in units of mag arcsec^{-2} , where $[8.0]$ is the core apparent magnitude at $8\mu\text{m}$.

Color-color plots in Figure 9 are not subject to the selection effects of unsharp masking (nor to distance effects) but nonetheless show a narrow range. The average values for the Vega-system colors and their dispersions σ for all the galaxies are $[3.6] - [4.5] = 0.21 \pm 0.007$, $\sigma([3.6] - [4.5]) = 0.53$, $[4.5] - [5.8] = 2.15 \pm 0.01$, $\sigma([4.5] - [5.8]) = 0.79$, and $[5.8] - [8.0] = 1.81 \pm 0.005$, $\sigma([5.8] - [8.0]) = 0.39$. These colors are the same as what we found for compact IRAC sources in the interacting galaxies NGC 2207 and IC 2163 (Elmegreen et al. 2006), and by unsharp masking using $8\mu\text{m}$ and $24\mu\text{m}$ images for M100 (Elmegreen et al. 2018).

The IRAC colors suggest that emission from extinguished photospheres makes $[3.6] - [4.5]$

²http://irsa.ipac.caltech.edu/data/SPITZER/docs/irac/irac_instrumenthandbook/

positive but low in the Vega system, combined with emission from PAHs to make $[5.8] - [8.0]$ high. Bare photospheric emission has a negative slope in the $3.6\mu\text{m}$ to $4.5\mu\text{m}$ range (Li & Draine 2001) with $[3.6] - [4.5] \sim -0.5$ in the AB system (e.g., Stern et al. 2005) and $[3.6] - [4.5] \sim 0$ in the Vega system (Allen 2004). Extinction is needed to bring the average color up to our measured Vega mag value of $[3.6] - [4.5] = 0.21 \pm 0.008$. Considering that a visual extinction of 30 mag produces a $[3.6] - [4.5]$ color excess between 0.4 and 0.45 depending on the extinction law (Megeath et al. 2004), the average visual extinction for our sources is about half of this, or ~ 15 mag. This extinction corresponds to a near-side gas mass surface density of $\Sigma_{\text{gas}} \sim 300 M_{\odot} \text{ pc}^{-2}$, using the local conversion factor between color excess and H I column density from Bohlin et al. (1978), $E(B - V) = N(\text{HI}) / (5.8 \times 10^{21} \text{ cm}^{-2})$, and a ratio of total-to-selective extinction $A_V / E(B - V) = 3.1$ with a mean molecular weight of 1.36 times the hydrogen mass. If the gas mass is the same on the far side of the extinguished source as on the near side, then the total gas mass surface density could be $\sim 600 M_{\odot} \text{ pc}^{-2}$. If an embedded source with this extinction and surface density occupies a fraction f of the $3''$ diameter of our photometry measurements, and the typical conversion to length is $\text{pc}/\text{arcsec} \sim 50$ from Table 1, then the corresponding gas mass is $\sim 10^7 f^2 M_{\odot}$.

Extinction barely affects the $[5.8] - [8.0]$ color (Allen 2004), so the IRAC emission from our sources also requires a significant excess at $8\mu\text{m}$. This could not from be Class II protostars, for example, which have extinguished photospheres and about the right $[3.6] - [4.5]$, because such protostars have disks that are too warm, making $[5.8] - [8.0]$ too blue: Allen (2004) and Megeath et al. (2004) show that Vega $[3.6] - [4.5] \sim 0 - 0.8$ and $[5.8] - [8.0] \sim 0.4 - 1.1$ for this class. They could be Class 0 protostars, which have extinguished photospheres with cool envelopes and disks; Whitney et al. (2003, see their Fig. 7) model low-inclination members of this class with $[3.6] - [4.5] \sim 0.5 - 0.9$ and $[5.8] - [8.0] \sim 1.2 - 1.5$. They also note that planetary nebulae and reflection nebulae have about the same colors. However, large dusty regions like we observe are not likely to have all their IRAC bands dominated by any of these sources, not the Class 0 because these stars are usually short-lived and rare compared to other classes, and not planetary or reflection nebulae.

A clue to the high $[5.8] - [8.0]$ color of our cores comes from whole galaxies, which have about the same value from PAH emission that peaks at $\sim 8\mu\text{m}$ (Stern et al. 2005; Winston et al. 2007; Gutermuth et al. 2009; Stutz et al. 2013). Galaxies have lower $[3.6] - [4.5]$ than the cores we observe because most of their photospheric emission is not highly extinguished. The most likely explanation for the observed core colors, considering the presence of our $8\mu\text{m}$ peaks in dust filaments, is that the low $[3.6] - [4.5]$ comes from extinguished photospheres of an embedded cluster, and the high $[5.8] - [8.0]$ comes from strong PAH emission on carbonaceous grains, which produce an emission bump at $6\mu\text{m}$ to $10\mu\text{m}$ (Li & Draine 2001).

Some galaxies like NGC 6946 also had a dozen or more peaks at $([3.6] - [4.5], [5.8] - [8.0]) \sim (0, 0)$ in Vega mag. These objects are likely stellar (Allen 2004), so we placed a lower cutoff at $[5.8] - [8.0] = 0.6$ to avoid them. Any core that had no measurable emission in one or more of the four IRAC bands was discarded as well.

In summary, the right-hand sides of Figures 3 to 7, and Tables 2 to 16, contain all of the small peaks that we examined on the unsharp mask images which have apparent $8\mu\text{m}$ magnitudes brighter than 16, measurable emission in each IRAC band, and a $[5.8] - [8.0]$ color that exceeds 0.6. This represents a total of 6315 objects.

4. Comparisons among different galaxies and spiral arm types

Comparison of the color IRAC images in Figure 1 and the unsharp mask images in Figures 3-7 shows how the unsharp mask images diminish the relative brightness of the main spiral arms and emphasize the bright and faint features equally. NGC 1566 and NGC 5194 are good examples, as the unsharp mask images barely show the well-known two-arm spirals that dominate the optical and near-infrared images.

There are other, more subtle, differences too, such as the small white dots that are in the unsharp mask images but indistinct in the IRAC color images. These are $8\mu\text{m}$ cores that are probably compact, highly-extincted regions of recent star formation (Sect. 3). Most of the thin spiral arms in all our galaxies have strings of cores all along their lengths. These cores are sometimes regularly spaced but not always. The spiral arm spurs generally have a few cores too, as do occasional rings in the outer regions, which might be supershells.

The cores are typically separated by 5 to 20 pixels ($3.75''$ to $15''$), with more cores in longer filaments. Intrinsic core sizes are not known because the $\sim 2.4''$ FWHM of the $8\mu\text{m}$ image typically corresponds to ~ 150 pc in these galaxies (see the scale in Table 1), and most embedded star-forming cores in resolved studies are smaller than this. Diffuse patches of emission in the unsharp mask images generally do not have cores, so a threshold surface density is apparently required to make them. The correspondence between the $8\mu\text{m}$ cores and the spiral arms and other features is discussed briefly here in order of NGC number for the galaxies.

As shown in Figure 3, NGC 628 is a multiple arm galaxy with strings of irregularly-spaced cores lying along all of the many arms and spurs and a few isolated cores between them in short filaments. NGC 1566 is a grand design galaxy in optical images and a multiple-arm galaxy in the unsharp mask image. It has cores along all of the thin arms and in several short spurs, but relatively few cores in the thick patches of diffuse emission. NGC 2403 is a

flocculent, low-mass galaxy with short spiral arms and a few irregularly spaced cores in each of them.

In Figure 4, NGC 3184 is a multiple arm galaxy with two long strings of cores in the inner arms and a few cores in spurs and irregular filaments between the arms. NGC 3351 is an inner ring galaxy with many arms. Few regular strings of $8\mu\text{m}$ cores appear, but the cores that are there are sprinkled throughout the arms and spurs. NGC 3938 is a multiple arm galaxy whose arms are filled with strings of cores. Very few show up between the main arms, except in spurs.

In Figure 5, NGC 4254 has multiple thick arms irregularly filled with cores. There are ring-like structures in the outer regions that also contain cores. NGC 4579 is a multiple arm galaxy with narrow arms sparsely filled with cores; there are relatively few spurs and most do not contain cores. NGC 4625 is a late-type multiple arm galaxy dominated by short arms, most of which have a few cores with relatively large separations.

In Figure 6, NGC 4725 has an inner ring and flocculent structure like 3351. There are long strings of cores along some of the arms and many short arms with just a few cores. NGC 4736 is an outer ring flocculent galaxy; its narrow arms are feathery and contain very few cores compared with all of the other galaxies in our sample. NGC 5194, a grand design galaxy dominated by two arms in the optical, appears as a multiple arm galaxy in this image. The two dominant arms are not obvious, and numerous cores are in both the arms and the spurs.

In Figure 7, NGC 5236 (with a streak coming from the $24\mu\text{m}$ image) is a multiple arm galaxy with many cores in the arms and very few between the arms. NGC 6946 is a multiple arm galaxy with bright arms in the color image but more irregular structure in the unsharp mask. There are many cores, both in the arms and spurs with mostly irregular spacings. NGC 7793, another flocculent low-mass galaxy, shows irregularly placed cores.

NGC 7793, NGC 2403, and NGC 6946 are all at about the same distance, where the photometric aperture used for the IR core measurements ($3''$) covers the same physical diameter, ~ 50 pc. The different numbers and distributions of $8\mu\text{m}$ cores in these galaxies are therefore not an artifact of distance. The most distant galaxy in our sample, NGC 4254, still shows $8\mu\text{m}$ cores lining the spiral arms.

The cores in the main arms of the two galaxies with the brightest two-arm spirals, NGC 1566 and NGC 5194, are brighter than the cores outside the arms. The brightness distributions of these spiral arm cores are shown in Figure 8 as red bars (these cores are also included in the total counts at these magnitudes, shown by the blue lines in the histogram). The average $8\mu\text{m}$ magnitude of 53 main spiral arm cores in NGC 1566 is 11.92 and the

average outside the main arms is 14.04. For 43 main arm cores in NGC 5194, these averages are 11.70 and 13.32. The magnitude of the average of the core fluxes (i.e., $-2.5 \log_{10}$ of the average of $10^{-0.4[8.0]}$ for magnitudes [8.0]) is 11.68 in the main arms of NGC 1566 and 12.94 outside the main arms. For NGC 5194, these are 11.41 and 12.62. Considering these latter averages, the ratio of core brightness in the arms to outside the arms is 3.2 and 3.0, respectively. The same ratio was found in M100 (Paper I). Star-forming regions in spiral arms are well known to be brighter and more massive than elsewhere (Rozas et al. 1996).

The similar appearance of the cores, nearly independent of distance, is partly a selection effect because all of the galaxies have about the same angular size and therefore pixel count in their diameters. The average and dispersion of the galaxy diameter distribution in pixels are 696 px and 281 px, respectively. Thus bigger galaxies have larger distances between the cores, making the images look similar. This scaling of galaxy morphology is a well-known phenomenon (e.g., Block 1984) and is not a bias in our selection of cores at the limiting magnitude. Bigger, more distant galaxies would presumably have more cores at fainter magnitudes than we can observe.

Figure 10 plots the inverse square root of the average density of cores in a galaxy, calculated as the number of cores divided by the area out to R_{25} , versus R_{25} . This abscissa is the average separation between cores. The linear relation in the figure shows that the average separation scales with the galaxy size, which is the same as saying that the number of chosen cores is about constant, as also evident from Table 1.

The approximately constant number of cores exceeding an apparent magnitude limit is consistent with a common luminosity function for equal-age star clusters, which is the same as the mass function. Suppose the luminosity function is $dn(L)/dL = n_0 L^{-2}$. If we define a maximum luminosity L_{\max} such that the integral over the luminosity function from L_{\max} to infinity is unity, then $n_0 = L_{\max}$. The total number of cores exceeding some minimum luminosity is

$$N(L > L_{\min}) = L_{\max} \int_{L_{\min}}^{\infty} L^{-2} dL = L_{\max}/L_{\min} \quad (1)$$

for $L_{\max} \gg L_{\min}$. At constant core density and constant core spacing, and with a constant minimum luminosity for core definition, this total number should increase with galaxy area, πR_{25}^2 for R_{25} in kpc. Now consider a limiting luminosity for observation, L_{obs} . For a fixed apparent magnitude, this limiting absolute luminosity increases as the square of the distance to the galaxy, D . The number of cores expected to be seen is thus

$$N(L > L_{\text{obs}}) = L_{\max} \int_{L_{\text{obs}}}^{\infty} L^{-2} dL = L_{\max}/L_{\text{obs}}. \quad (2)$$

The numerator in this expression increases as R_{25}^2 and the denominator increases as D^2 . For

an approximately constant galaxy angular size, as is typically chosen for surveys, $R_{25} \propto D$. Thus, the number of cores above a fixed apparent magnitude is independent of distance, and their average spacing scales with the galaxy size. This result implies that if one of our distant galaxies could be observed closer, it would have a larger angular size and more cores above our fixed apparent magnitude limit. Also, the intrinsically fainter cores (not visible in our survey with the true galaxy distance) would probably be located between the cores we observe now in the distant galaxy, with a shorter spacing between them, measured in kpc, for the nearby version.

Also because of the limited angular resolution, the cores could be subdivided into multiple molecular clouds and star-forming regions. The lack of specific optical emission from many of these cores suggests that even if they are fragmented, they are still unlikely to have a high fraction of their young stars in the low-extinction regions between the fragments.

5. Implications for Star Formation

5.1. Spiral Arms

The core colors in IRAC (Fig. 9) suggest highly embedded star formation with significant PAH emission (Sect. 3). Because many are located in dust ridges on the inner parts of spiral arms, they are probably evidence for star formation initiated by a density wave shock, as suggested in general terms by Roberts (1969). There are many early models for how such triggering might occur, including cloud collisions (Kwan & Valdes 1983; Scoville et al. 1983) and the Parker instability (Mouschovias et al. 1974), but the occasional appearance of regularity and the relative importance of gravity in the Parker-Jeans instability (Elmegreen 1982; Chou et al. 2000) suggests they formed by some mixture of agglomeration and magneto-gravitational instabilities in the dense gas. Presumably the embedded stars will break out of their clouds, estimated above to have a mean visible extinction of ~ 15 mag on the near side of the galaxy disk, and then they will become visible as HII regions, OB associations and young optical clusters. Subsequently, they will age as they move downstream from the shock, causing a blue-to-red color gradient, as found in some cases (e.g., Martínez-García et al. 2009; Shabani et al. 2018; Peterken et al. 2019; Yu & Ho 2019).

This standard scenario is not always expected. Some spiral arms are not quasi-stationary stellar waves, as envisioned by Lin and Shu, but transient spirals growing from two-dimensional disk instabilities and wrapping up in a shear flow (e.g., Baba et al. 2013). Then the gas and young stars do not move much relative to the stellar spiral as they age, and color gradients should be small or even reversed (Dobbs & Pringle 2010; Shabani et al. 2018).

Because we find $8\mu\text{m}$ cores in spiral arm spurs and at shell edges downstream from the main dust lanes (Sect. 4), star formation continues even as the gas moves through the arm. Obviously, this decreases the average age gradient too, producing young stars all throughout the spiral and even in the trailing interarm region. The 8μ cores in spurs and shells also suggest a likely role for self-gravity in forming these objects.

Most $8\mu\text{m}$ cores are not regularly spaced along their dusty filaments, although some are over short segments (see Figs. 3-7). Regions with regular spacing suggest an instability or forced-agglomeration of smaller clouds, with a spacing at the fastest growing mode along the filament (Sect. 1). They also suggest that the whole segment with the regularity started this process at about the same time. Otherwise, the filaments should be more irregular with the youngest regions forming wherever the gas is just now building up and the older regions empty where a previous generation just broke out. This lack of simultaneity could be the reason most filaments do not have regularly spaced cores.

Transient spirals also prolong the time when the gas is dense and can form condensations by instabilities. In the model by Dobbs & Bonnell (2008), the gas collected in the arms and stayed there while the spiral grew and moved. There was no age gradient and no spurs because there was no downstream flow of the gas through the arms.

5.2. A possible connection to the Jeans mass

To determine whether the $8\mu\text{m}$ core luminosities might be related to a gravitational Jeans mass, we plotted the core magnitudes versus the distances from the galaxy’s centers. The approximately exponential decrease in gas surface density with radius, $\Sigma_{\text{gas}}(R)$, and the relatively constant gas thickness before the outer flare region ($H(R)$, Wilson et al. 2019), suggests the Jeans mass, which is approximately $\Sigma_{\text{gas}}H^2$, should decrease with galactocentric radius. Figure 11 shows the results for our cores. Red points are for spiral arm cores, as also distinguished by red histograms in Figure 8. There is a large range of core magnitudes for most galaxies in the outer regions, but only bright cores are in the inner regions, considering the radial trend in the lower envelop of points. This trend is consistent with the expected trend in Jeans mass, but it may also arise from a selection effect where faint cores in the inner regions do not stand out significantly above the brighter disks there and so are not selected in our survey. The unsharp mask technique makes the average core backgrounds uniform, but not the noise in those backgrounds, which scales approximately with the square root of the pixel count. The actual trend in the figure looks more like the effect of a Jean’s mass, however. Typically the faintest magnitude varies by 4 magnitudes from the inner to the outer region, and for most galaxies, this radial span corresponds to around 4 exponential

scale lengths. Since each scale length is one exponential factor and also about one magnitude, the decline in luminosity is approximately proportional to the surface density. This is the relationship for the Jeans mass given above. The variation would be closer to 2 magnitudes if it were proportional to the square root of the surface density in the case of noise limitations. Also in the noise interpretation, the lack of bright cores in the outer regions would have to be explained for, e.g. NGC 1566, where the upper envelope of the points has a trend with galactocentric distance also.

The clumps in the main spiral arms of NGC 1566 get somewhat brighter with radius, unlike the other distributions in Figure 11. For NGC 5194, the arms have no obvious trend. The trend for NGC 1566 suggests that the disk thickness in the arms increases with radius, possibly from a more constant velocity dispersion. When the velocity dispersion is constant, both the thickness and the Jeans mass vary as the inverse of the surface density (Inoue & Yoshida 2018). This is consistent with the trend we observe for the spiral arms in NGC 1566.

5.3. A possible connection to the star formation rate

The total luminosity and stellar mass of the $8\mu\text{m}$ clumps should be proportional to the galaxy SFR if the clumps are the youngest stages of star formation. Figure 12 shows this is the case. On the left, the SFRs from Table 1 are plotted versus the summed $8\mu\text{m}$ luminosities, converted to absolute magnitudes (i.e., $-2.5 \log_{10}$ of the sum over all cores of $10^{-0.4[8.0]}$ for apparent magnitude [8.0], converted to absolute magnitude by the subtraction of $5 \log_{10}(10^5 D)$ for distance D in Mpc). Galaxies with higher total SFRs have greater summed $8\mu\text{m}$ luminosities of the cores. Note that this is not the total $8\mu\text{m}$ luminosity of the galaxy, but only the sum of the relatively small core regions.

Figure 12(b) converts the IRAC luminosities into approximate stellar masses using the procedure in Paper I. That is, the sum of the luminosities of the four IRAC bands is multiplied by 10 to obtain an estimate of the total infrared luminosity, based on integrals over SEDs for starbursts in Xu et al. (2001). This total clump IR luminosity is then converted to stellar mass of young stars using the bolometric magnitude of a young stellar population in Bruzual & Charlot (2003), which is -2.7944 for solar metallicity at less than 1 Myr age. Using 4.74 mag as the bolometric magnitude of the Sun, the bolometric luminosity per solar mass of young stars is $3.01 \times 10^{35} \times 10^{0.4*2.7944}$ at 1 Myr age. The inferred stellar mass is the total IR luminosity of the clump divided by this quantity. The stellar masses would be larger by a factor 5.1 for an age of 10 Myr.

Figure 12(b) shows, like Figure 12(a), the importance of $8\mu\text{m}$ clumps increasing with the SFR. With the clump mass, however, we can divide the abscissa by the ordinate and get a time scale. This time would be the average age of the clumps if all of the star formation in the galaxy came from them. Considering the fainter clumps that are not included (cf. Fig. 8) and the typical mass distribution for star forming regions, i.e., varying as the inverse of mass for equal logarithmic intervals of mass, there could be an approximately equal amount of clump mass in addition to what is plotted in Figure 12(b), which would double the timescale. With this factor, the time is between 0.2 Myr and 2 Myr, which is a reasonable age for a mostly-embedded young stellar population. This result suggests that most of the star formation in these galaxies goes through a phase when it is embedded in a dense $8\mu\text{m}$ clump like what we observe. This is an earlier phase than an HII region or FUV source, but the $\text{H}\alpha$ or FUV luminosities can give about the same SFRs because they sample a different time in the evolution of the clumps. The $24\mu\text{m}$ luminosities presumably sample both this embedded phase and a later, more exposed phase, but the $24\mu\text{m}$ images do not have the angular resolution to see the $3''$ diameter cores that are visible at $8\mu\text{m}$.

6. Conclusions

An unsharp mask technique has revealed several hundred small $8\mu\text{m}$ cores in each of 15 spiral galaxies observed with the Spitzer Space telescope. The cores have colors suggestive of embedded star formation beneath ~ 15 mag of visual extinction combined with bright PAH emission. Nearly all spiral arms and spurs have several IR cores, and more occur singly in smaller dust patches. Most cores do not correspond to obvious optical features because of the extinction, and neither do they stand out in the $8\mu\text{m}$ or color Spitzer images because of confusion with lower-intensity backgrounds.

The present study follows a more thorough view of similar cores in the galaxy M100, published earlier (Elmegreen et al. 2018). The core colors there are about the same as those here, as are the apparent magnitudes, which are set by selection effects. We expect many more such cores will be found at higher resolution and greater sensitivity. The usual luminosity function for young stellar clusters suggests that all star-forming galaxies selected for angular size will have about the same number and angular spacings for their $8\mu\text{m}$ cores if observed to the same apparent magnitude limit. That is the case here.

The morphological similarity between the observed galactic $8\mu\text{m}$ cores with their surrounding filaments and star-forming cores and filaments in the solar neighborhood suggests a universal process of core formation based on gravitational collapse in thin compressed regions. For galaxies, the compression on the largest scale is from stellar spiral wave activity.

Because the interstellar medium on this large scale is generally composed of smaller diffuse and self-gravitating clouds, the cores that form would also involve some agglomeration of these smaller clouds, forced somewhat by their mutual gravitational attraction. Other cores that are visible in $8\mu\text{m}$ rings in the outer parts of our galaxies also suggest gas compression and collapse initiated by stellar feedback.

The positions of these cores inside spiral shock fronts suggests they are the first step in the star formation process connected with spiral waves. When the young stars emerge from their current high extinctions, they will presumably produce the usual optical structures and age gradients that are seen in spiral arms.

The summed core luminosities and equivalent stellar masses correlate well with the total galaxy star formation rates. The embedded stellar masses could account for the star formation rate if the evolution phase of a typical core is between 0.2 Myr and 2 Myr. This result suggests that most star formation goes through a dense $8\mu\text{m}$ core phase and that we are observing most of the young intermediate-to-high mass star-formation sites in these galaxies.

Final note: This paper is dedicated to our friend and colleague for 27 years, Dr. Yuri Nicolaevich Efremov (1937-2019), of the Sternberg Astronomical Observatory in Moscow.

We are grateful to the referee for useful comments.

REFERENCES

- Allen, L., Calvet, N., D'Alessio, P., Merin, B., Hartmann, L., et al. 2004, *ApJS*, 154, 363
- André, P. 2017, *CRGeo*, 349, 187
- Baba, J., Saitoh, T.R., & Wada, K. 2013, *ApJ*, 763, 46
- Balbus, S.A. 1988, *ApJ*, 324, 60
- Balbus, S. A., & Cowie, L. L. 1985, *ApJ*, 297, 61
- Block, D. L. 1984, in *A photographic atlas of primarily late type spirals printed as if each galaxy were at the same distance*, Fort Hare University Press, South Africa. 36 pp.
- Bohlin, R. C., Savage, B. D., & Drake, J. F. 1978, *ApJ*, 224, 132
- Bruzual, G., & Charlot, S. 2003, *MNRAS*, 344, 1000
- Chakrabarti S., Laughlin G., & Shu F. H., 2003, *ApJ*, 596, 220

- Chandrasekhar, S. & Fermi, E. 1953, ApJ, 118, 116
- Chira, R. -A., Kainulainen, J., Ibáñez-Mejía, J. C., Henning, Th., Mac Low, M. -M. 2018, A&A, 610, A62
- Chou, W., Matsumoto, R., Tajima, T., Umekawa, M., & Shibata, K. 2000, ApJ, 538, 710
- Clarke, S. D., Whitworth, A. P., Duarte-Cabral, A., & Hubber, D. A. 2017, MNRAS, 468, 2489
- Cowie, L. L. 1981, ApJ, 245, 66
- Dobbs, C.L. & Bonnell, I.A. 2008a, MNRAS, 385, 1893
- Dobbs, C.L. 2008, MNRAS, 391, 844
- Dobbs C. L. & Pringle J. E., 2010, MNRAS, 409, 396
- Dobbs C. & Baba J. 2014, PASA, 31, 35
- Efremov, Yu. N. 2010, MNRAS, 405, 1531
- Elmegreen, B.G. 1979, ApJ, 231, 372
- Elmegreen, B.G. 1982. ApJ, 253, 634
- Elmegreen, B.G., & Elmegreen, D.M. 1983, MNRAS, 203, 31
- Elmegreen, B.G., & Elmegreen, D.M. 1986, ApJ, 311, 554
- Elmegreen, B.G. & Elmegreen, D.M. 1987, ApJ, 320, 182
- Elmegreen, D.M. & Elmegreen, B.G. 1987, ApJ, 314, 3
- Elmegreen, B.G. 1994, ApJ, 433, 39
- Elmegreen, B.G., Elmegreen, D.M., & Efremov, Y.N 2018, ApJ, 863, 59
- Elmegreen, D.M., Elmegreen, B.G., Kaufman, M., et al. 2006, ApJ, 642, 158
- Fiege, J.D. & Pudritz, R.E. 2000, MNRAS, 311, 105
- Goldreich, P., & Lynden-Bell, D. 1965, MNRAS, 130, 97
- Goodman, A.A., Alves, J., Beaumont, C.N., et al. 2014, ApJ, 797, 53
- Grabelsky, D. A., Cohen, R. S., Bronfman, L., Thaddeus, P., & May, J. 1987, ApJ, 315, 122

- Gusev, A. S., & Efremov, Yu. N. 2013, MNRAS, 434, 313
- Gutermuth, R. A., Megeath, S. T., Myers, P. C., et al. 2009, ApJS, 184, 18
- Hosseini-rad, M., Abbassi, S., Roshan, M., Naficy, K. 2018, MNRAS, 475, 2632
- Inoue, S. & Yoshida, N. 2018, MNRAS, 474, 3466
- Inoue, S. & Yoshida, N. 2019, MNRAS, 485, 3024
- Inutsuka, S. & Miyama, S.M. 1992, ApJ, 388, 392
- Kainulainen, J., Hacar, A., Alves, J., Beuther, H., Bouy, H., & Tafalla, M. 2016, A&A, 586, A27
- Kennicutt, R.C., Jr., Armus, L., Bendo, G. et al. 2003, PASP, 115, 928
- Kennicutt, R.C., Calzetti, D., Aniano G., et al. 2011, PASP, 123, 1347
- Khoperskov S. A., Vasiliev E. O., Sobolev A. M., & Khoperskov A. V., 2013, MNRAS, 428, 2311
- Kim, W.-T., & Ostriker, E.C. 2001, ApJ, 559, 70
- Kim, W.-T., Ostriker, E.C., & Stone, J.M. 2002, ApJ, 581, 1080
- Kim, W.-T., & Ostriker, E.C. 2002b, ApJ, 570, 132
- Kim, T.-T., & Ostriker, E.C. 2006, ApJ, 646, 213
- Kim, W.-T., & Ostriker, E.C. 2007, ApJ, 660, 1232
- Koo, B.-C., Park, G., Kim, W.-T., Lee, M.G., Balser, D., Wenger, T. 2018, AAS, 23123704
- Kratter, K., & Lodato, G. 2016, ARA&A, 54, 271
- Kwan, J. & Valdes, F. 1983, ApJ, 271, 604
- Lee, W.-K., & Shu, F.H. 2012, ApJ, 756, 45
- Li, A., & Draine, B.T. 2001, ApJ, 554, 778
- Lou, Y.-Q. & Hu, X.Y. 2017, MNRAS, 468, 2771
- Martínez-García, E. E., González-Lópezlira, R.A., Bruzual, A.G., 2009, ApJ, 694, 512
- Mattern, M., Kainulainen, J., Zhang, M., & Beuther, H. 2018, A&A, 616, A78

- Megeath, S.T., Allen, L.E., Gutermuth, R.A., Pipher, J. L., Myers, P.C., Calvet, N., Hartmann, L., Muzerolle, J., & Fazio, G. G. 2004, *ApJS*, 154, 367
- McGee, R. X. & Milton, J. A. 1964, *AuJPh*, 17, 128
- Mouschovias, T. Ch., Shu, F. H., Woodward, P. R. 1974, *A&A*, 33, 73
- Nagasawa, M. 1987, *Prog. Theor. Phys.*, 77, 635
- Nakamura, F., Hanawa, T., & Nakano, T. 1993, *PASJ*, 45, 551
- Peterken, T.G., Merrifield, M.R., Aragón-Salamanca, A., Drory, N., Krawczyk, C.M., Masters, K.L., Weijmans, A.-M., Westfall, K.B. 2019, *NatAs*, 3, 178
- Ragan S. E., Henning T., Tackenberg J., et al. 2014, *A&A*, 568, A73
- Renaud, F., Bournaud, F., Emsellem, E., et al. 2013, *MNRAS*, 436, 1836
- Renaud, F., Bournaud, F., Emsellem, E., Elmegreen, B., & Teyssier, R. 2014, *ASPC*, 480, 247
- Roberts, W.W. 1969, *ApJ*, 158, 123
- Rossano, G. S. 1978, *AJ*, 83, 234
- Rozas, M., Beckman, J. E., Knapen, J. H. 1996, *A&A*, 307, 735
- Schneider, S., & Elmegreen, B.G. 1979, *ApJS*, 41, 87
- Scoville, N. Z., Sanders, D. B., Clemens, D.P. 1986, *ApJ*, 310, L77
- Seo, Y.M. & Youdin, A.N. 2016, *MNRAS*, 461, 1088
- Shabani, F., Grebel, E.K., Pasquali, A. et al. 2018, *MNRAS*, 478, 3590
- Shetty R., & Ostriker E. C., 2006, *ApJ*, 647, 997
- Shu F. H., 2016, *ARA&A*, 54, 667
- Stern, D., Eisenhardt, P., Gorjian, V. et al. 2005, *ApJ*, 631, 163
- Stodólkiewicz, J.S. 1963, *Acta. Astron.* 13, 30
- Stutz, A., Tobin, J., Stanke, T., Megeath, T., Fischer, W. et al. 2013, *ApJ*, 767, 36
- Thilker, D.A., Bianchi, L., Meurer, G. et al. 2007, *ApJS*, 173, 538

Tomisaka, K. 1987, PASJ, 39, 109

Tomisaka, K. 1995, ApJ, 438, 226

Toomre, A. 1981, in: The structure and evolution of normal galaxies, eds. S. M. Fall & D. Lynden-Bell, Cambridge University Press, 111

Yu, S.-Y., & Ho, L.C. 2019, ApJ, 871, 194

Wada K. & Koda J., 2004, MNRAS, 349, 270

Whitney, B. A., Wood, K., Bjorkman, J. E., & Cohen, M. 2003, ApJ, 598, 1079

Wilson, C.D., Elmegreen, B.G., Bemis, A., & Brunetti, N. 2019, ApJ, 882, 5

Winston, E., Megeath, S. T., Wolk, S. J., et al. 2007, ApJ, 669, 493

Xu, C., Lonsdale, C.J., Shupe, D.L., O’Linger, J., & Masci, F. 2001, ApJ, 562, 179

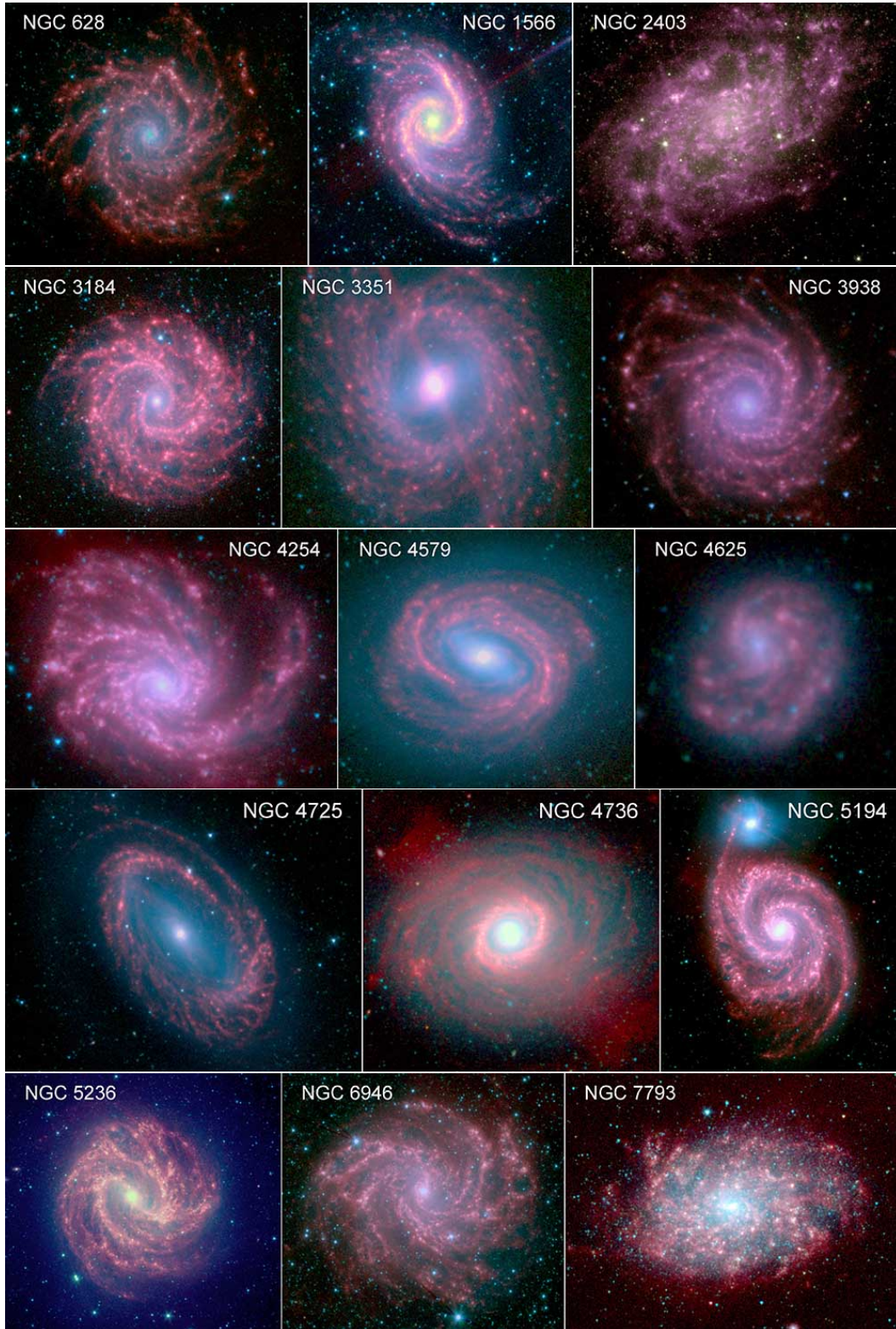


Fig. 1.— Color IRAC images of the 15 galaxies in this study from composites of $3.6\mu\text{m}$ (in blue), $4.5\mu\text{m}$ (in green), and $8\mu\text{m}$ (in red) images. [Figure quality reduced for arXiv.]

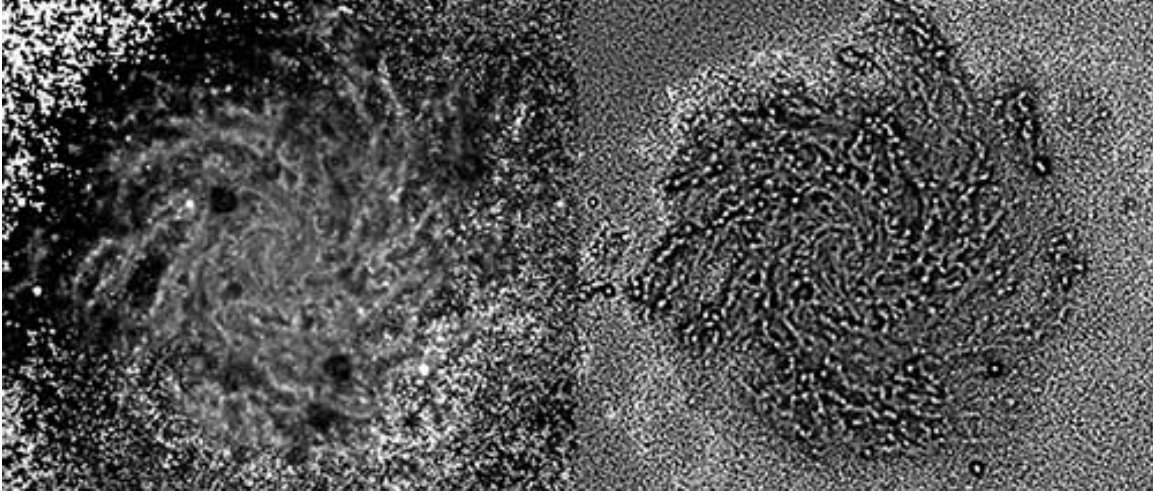


Fig. 2.— Unsharp masks made by dividing the $8\mu\text{m}$ image of NGC 628 by the $24\mu\text{m}$ image (left) and by dividing the same $8\mu\text{m}$ image by a Gaussian-blurred version of the $8\mu\text{m}$ image (right). The version on the right has better definition of the clumps, so we use that technique here. [Figure quality reduced for arXiv.]

Table 1. Galaxies

NGC	Distance (GSR), Mpc	Distance Modulus	No. of Cores	Hubble type	Arm Class	R_{25} arcmin	R_{25} kpc	pc per arcsec	SFR $M_{\odot} \text{ yr}^{-1}$
628	11.13	30.23	681	SA(s)c I	M	5.24	16.90	53.80	1.6
1566	19.63	31.46	403	SAB(s)bc I	G	4.16	23.67	94.88	8.8
2403	3.39	27.65	499	SAB(s)cd III	F	10.94	10.75	16.39	1.0
3184	8.8	29.72	416	SAB(rs)cd II.2	M	3.71	9.46	42.53	0.074
3351	9.98	30.00	324	SB(r)b II	M	3.71	10.73	48.24	0.66
3938	12.52	30.49	353	SA(s)c I	M	2.69	9.75	60.51	0.87
4254	34.73	32.70	469	SA(s)c I.3	M	2.69	27.04	167.86	22.8
4579	21.62	31.67	179	SAB(rs)b II	M	2.94	18.46	104.50	1.9
4625	9.88	29.97	69	SAB(rs)m pec V	F	1.09	3.13	47.75	0.059
4725	17.8	31.25	272	SAB(r)ab pec II	M	5.36	27.66	86.03	0.98
4736	5.31	28.63	169	(R)SA(r)ab I-II	F	5.61	8.64	25.67	0.49
5194	8.12	29.55	670	SA(s)bc pec I-II	G	5.61	13.21	39.25	7.8
5236	5.63	28.75	857	SAB(s)c II	M	6.44	10.52	27.21	9.0
6946	3.93	27.97	725	SAB(rs)cd II	M	5.74	6.54	19.00	2.4
7793	3.38	27.65	229	SA(s)d IV	F	4.67	4.57	16.34	0.26

¹Star formation rates are from $\text{H}\alpha$ and $24\mu\text{m}$ in Kennicutt et al. (2011) in all cases but NGC 1566, NGC 2403, NGC 5194, and NGC 5236, where they are from FUV and total IR in Thilker et al. (2007).

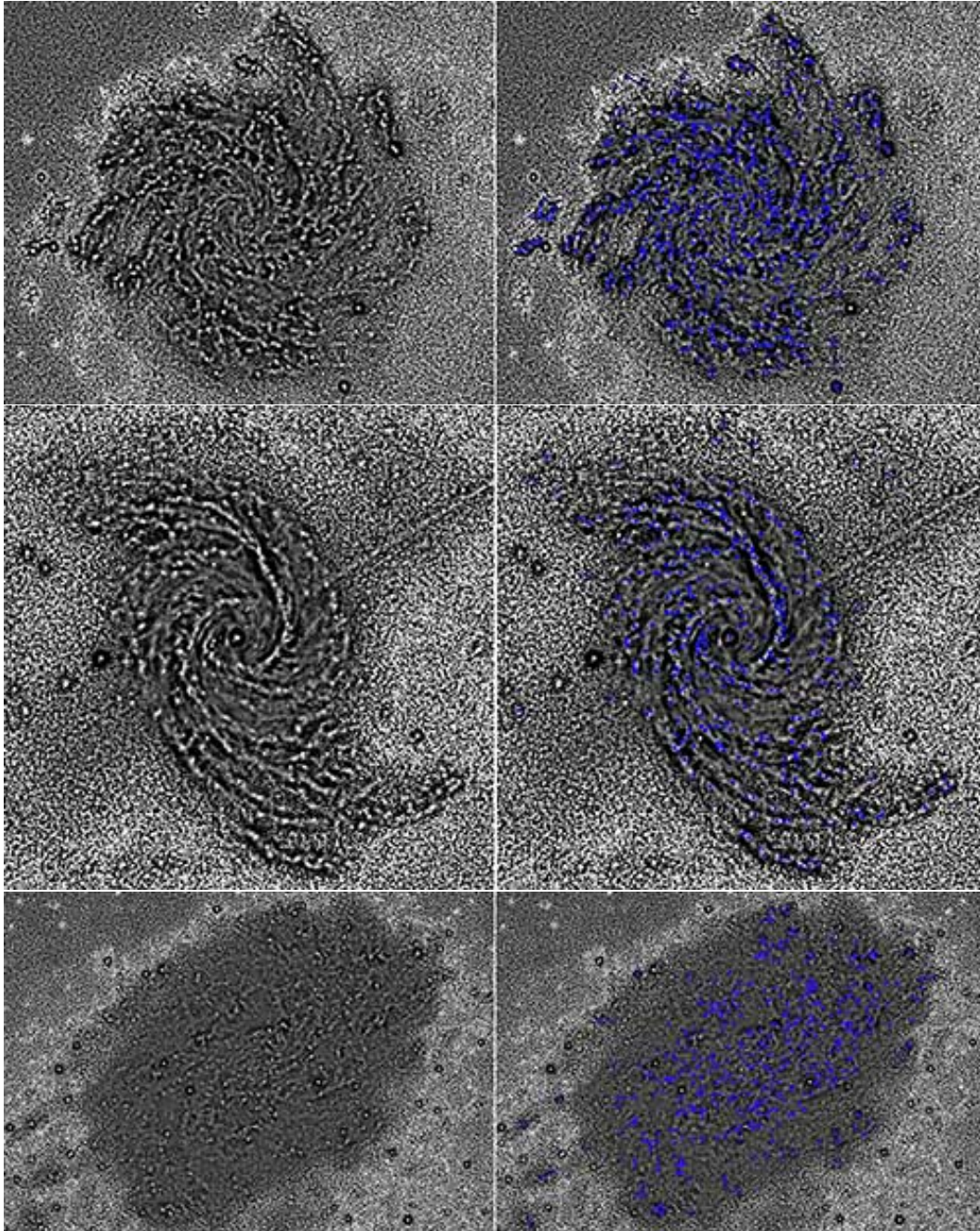


Fig. 3.— Unsharp mask images of NGC 628 (top), NGC 1566 (middle), and NGC 2403 (bottom). The figures on the right show blue dots for the chosen cores that are also listed in the tables. These cores have an apparent $8\mu\text{m}$ magnitude brighter than 16 mag and a $[3.4] - [4.5]$ color greater than 0.6 to avoid unextincted stars. Star-like objects with no blue dots have been excluded because of one of these three criteria. [Figure quality reduced for arXiv.]

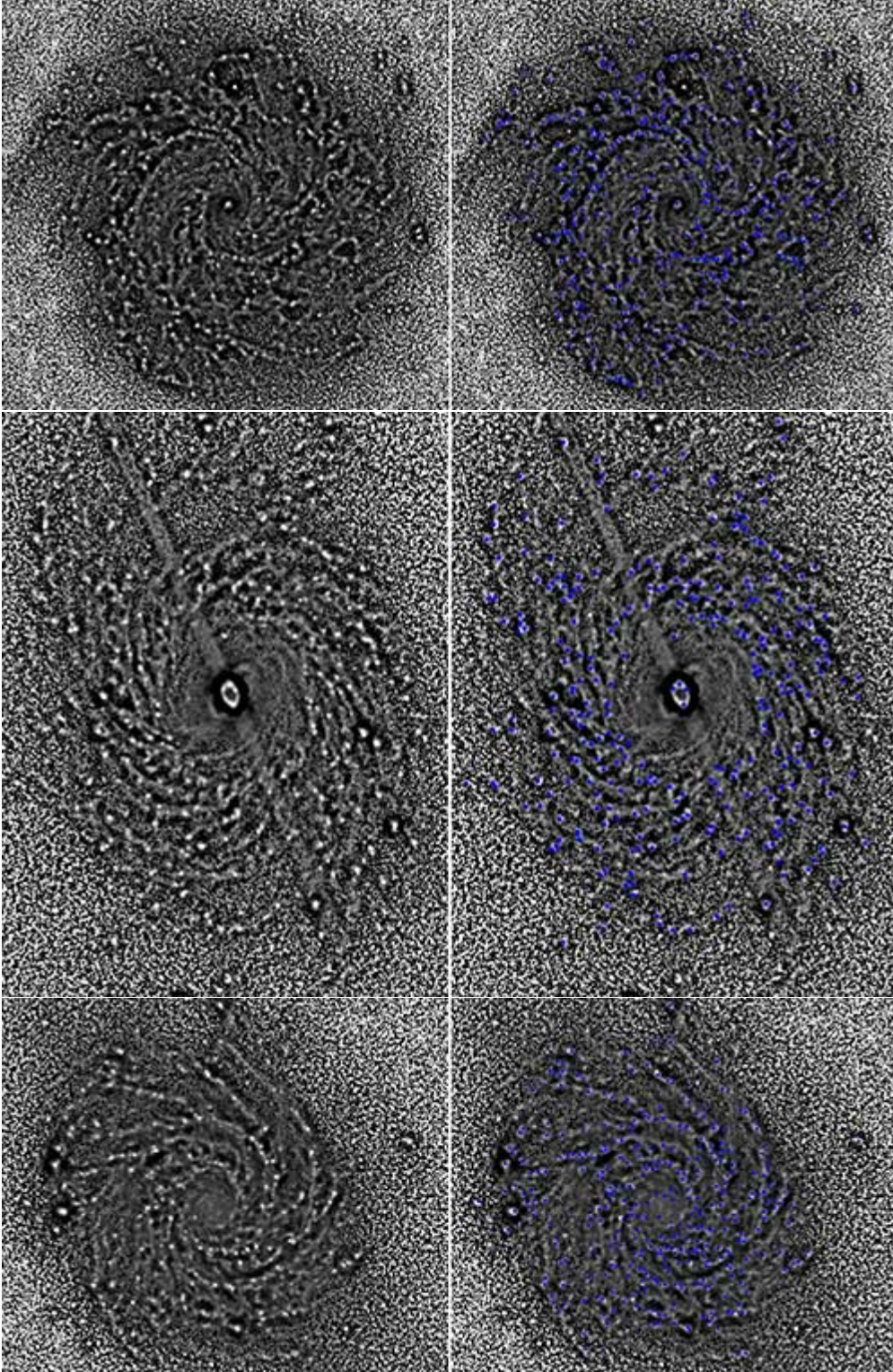


Fig. 4.— Unsharp mask images of NGC 3184 (top), NGC 3351 (middle), and NGC 3938 (bottom). [Figure quality reduced for arXiv.]

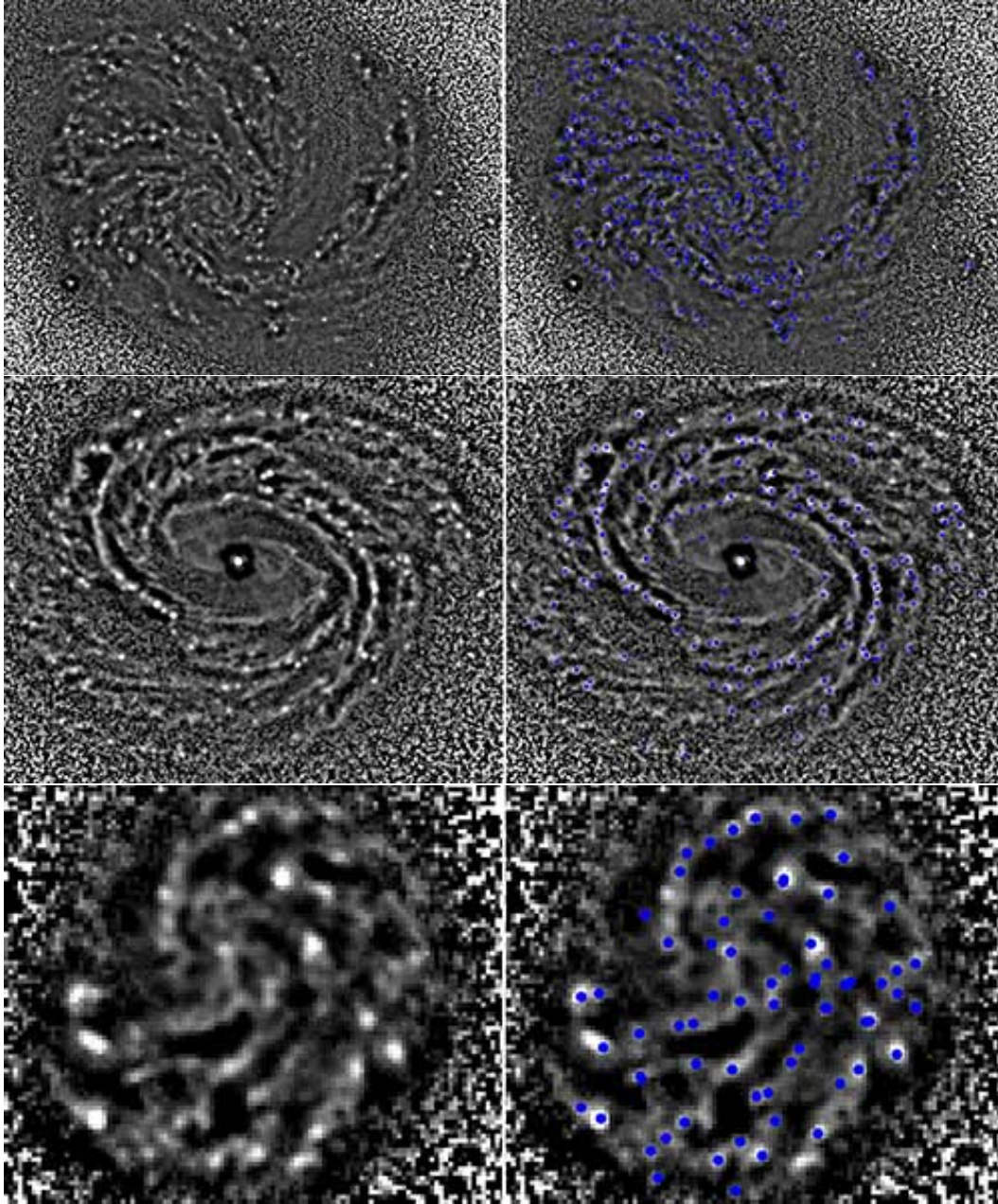


Fig. 5.— Unsharp mask images of NGC 4254 (top), NGC 4579 (middle), and NGC 4625 (bottom). [Figure quality reduced for arXiv.]

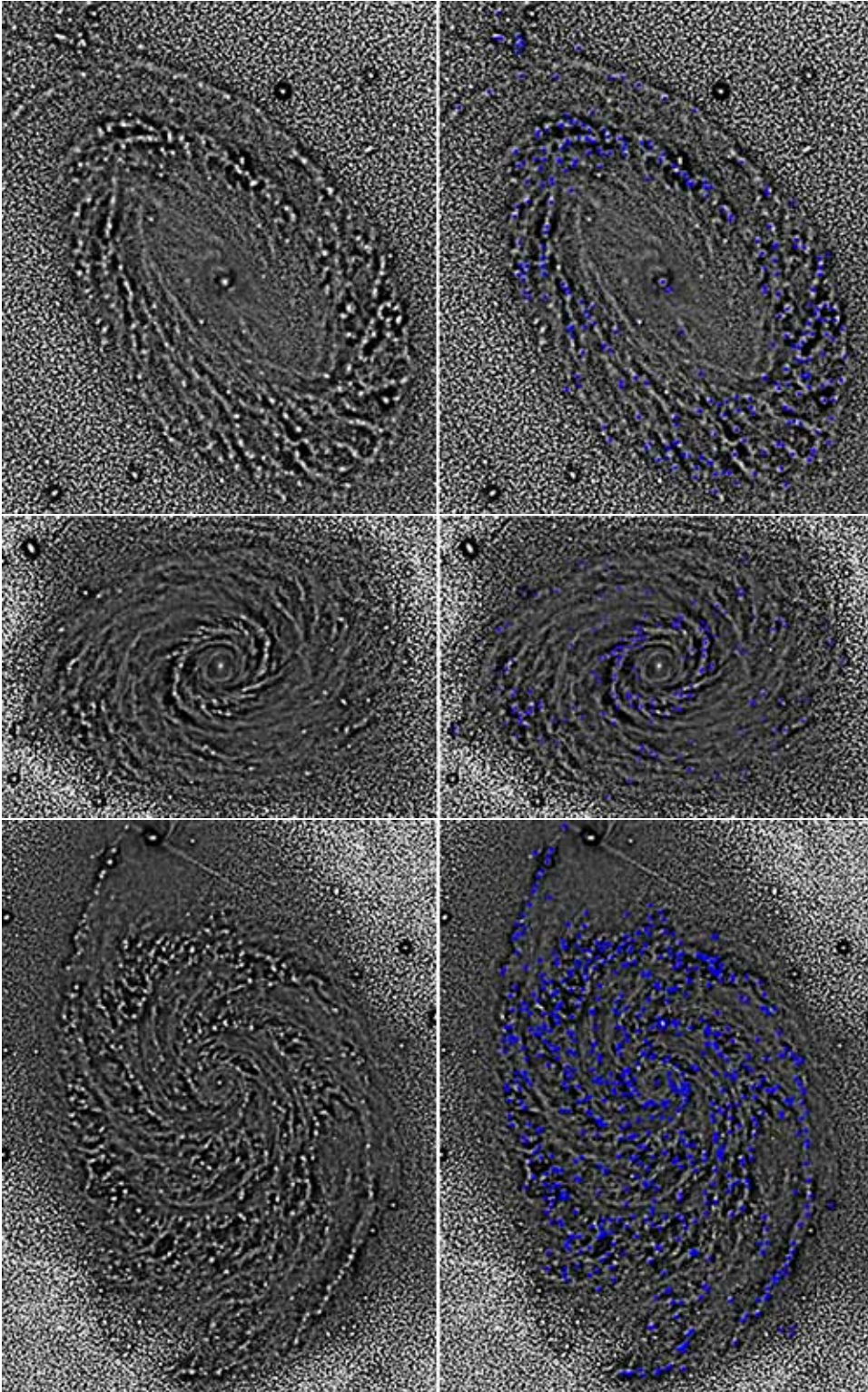


Fig. 6.— Unsharp mask images of NGC 4725 (top), NGC 4736 (middle), and NGC 5194 (bottom). [Figure quality reduced for arXiv.]

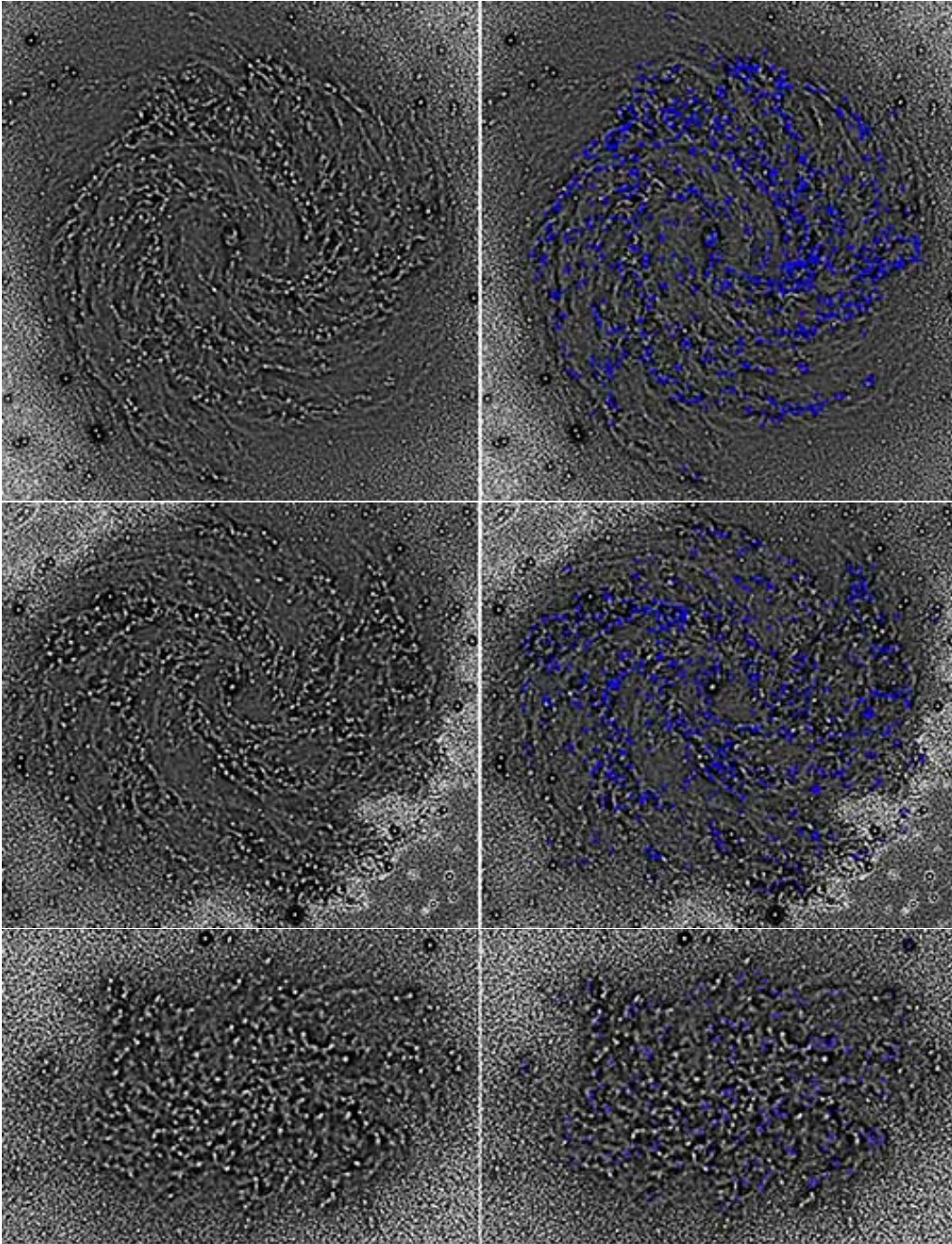


Fig. 7.— Unsharp mask images of NGC 5236 (top), NGC 6946 (middle), and NGC 7793 (bottom). [Figure quality reduced for arXiv.]

